

Article

Mesospheric Gravity Wave Potential Energy Density Observed by Rayleigh Lidar above Golmud (36.25° N, 94.54° E), Tibetan Plateau

Weibo Zhao ^{1,2,*}, Xiong Hu ¹ , Weilin Pan ^{2,3}, Zhaoai Yan ^{1,2} and Wenjie Guo ¹

¹ National Space Science Center, Chinese Academy of Sciences, Beijing 100190, China; xhu@nssc.ac.cn (X.H.); yanza@nssc.ac.cn (Z.Y.); guowenjie@nssc.ac.cn (W.G.)

² College of Earth Sciences, University of Chinese Academy of Sciences, Beijing 101499, China; panweilin@mail.iap.ac.cn

³ Institute of Atmospheric Physics, Chinese Academy of Sciences, Beijing 100029, China

* Correspondence: zhaoweibo19@mails.ucas.ac.cn

Abstract: Rayleigh lidar data in 2013–2015 is used to describe the characteristics of gravity wave potential energy density in the mesosphere above Golmud (36.25° N, 94.54° E) of the Tibetan Plateau. In this study, the vertical profiles of the atmospheric gravity wave potential energy density between 50–80 km above the region are presented, including the potential energy mass density E_{pm} and the potential energy volume density E_{pv} . It shows the mathematical characteristics of the atmospheric gravity wave potential energy density vertical distribution, which also indicate the gravity waves are obviously dissipated in the lower mesosphere and close to conservative growth in the upper mesosphere (the turning point is around 61 km). A total of 1174 h of data covers seasonal changes, which reveals the seasonal characteristics of the potential energy density. The E_{pm} increases faster with altitude in summer than others. All seasons of the potential energy density profiles show that gravity waves are dissipated in the lower mesosphere, among which spring and winter are the most severe and summer is weakest. The E_{pm} is higher in spring and winter below 55 km. Above 55 km, it is the maximum in winter, followed by summer. Then, the AGWs activities between the location with mid-latitudes and different longitudes are compared and discussed.

Keywords: atmospheric gravity waves; Rayleigh lidar; potential energy density; mesospheric dynamics



Citation: Zhao, W.; Hu, X.; Pan, W.; Yan, Z.; Guo, W. Mesospheric Gravity Wave Potential Energy Density Observed by Rayleigh Lidar above Golmud (36.25° N, 94.54° E), Tibetan Plateau. *Atmosphere* **2022**, *13*, 1084. <https://doi.org/10.3390/atmos13071084>

Academic Editors: Goderdzi Didebulidze and Sergey P. Kshevetskii

Received: 13 June 2022

Accepted: 7 July 2022

Published: 9 July 2022

Publisher's Note: MDPI stays neutral with regard to jurisdictional claims in published maps and institutional affiliations.



Copyright: © 2022 by the authors. Licensee MDPI, Basel, Switzerland. This article is an open access article distributed under the terms and conditions of the Creative Commons Attribution (CC BY) license (<https://creativecommons.org/licenses/by/4.0/>).

1. Introduction

Atmospheric gravity waves (AGWs) play a major role in atmospheric circulation, vertical structural coupling [1,2] and chemical composition transport [3–5] and have always been a hot topic regarding the middle and upper atmosphere. In numerical weather prediction and climate simulation models, AGW parameterizations are required to simulate the impact of AGWs on the atmosphere. However, the imperfect parameterization schemes bring challenges to the accuracy of atmospheric models [6,7]. More observations are beneficial to the description and validation of the drag effect of AGWs in the parameterization schemes. Satellite and ground-based atmospheric temperature data were used to derive the gravity wave potential energy density (GWPED) [8,9], which is usually used to measure the strength of AGWs' activity. The vertical profiles of GWPED can effectively reflect the altitude regions and degree of wave dissipation. They can also help evaluate the momentum flux of AGWs, which is a key component for observation, as well as parameterization [10–12].

Lidar has the characteristics of high spatial and temporal resolution, which are widely used to observe medium- and low-frequency AGWs from the troposphere up to the lower thermosphere. The rotational Raman lidar is used for the measurement of AGWs in the

troposphere and lower stratosphere [13,14]. Because of signal contamination from aerosols, the Rayleigh lidar at 532 nm is used for studying the AGWs in the stratosphere and mesosphere [15,16]. In the mesosphere and lower thermosphere (MLT), Fe Boltzmann lidar, Na resonance fluorescence lidar and K resonance fluorescence lidar are widely used [13,14,17,18]. Accumulated Rayleigh lidar data have been used to investigate the characteristics of GWPED, including in low-latitude [19,20], mid-latitude [21–29] and high-latitude regions [30–39]. GWPED exhibits different characteristics in different regions, such as the magnitude and growth rates of GWPED, the dissipation altitudes and degree of AGWs, and the dependence on seasonal variations.

This study is based on the 532 nm Rayleigh lidar data of the MARMOT (Middle Atmosphere Remote Mobile Observatory in Tibet) system to survey the characteristics of GWPED in the mesosphere (50–80 km) above Golmud (36.25° N, 94.54° E). It is the first time Rayleigh lidar has been used to research the annual and seasonal variations in GWPED in the mesosphere above the Tibetan Plateau, the third pole of the world. The paper is organized as follows: Section 2 presents the lidar system, data and analysis methods. Section 3 presents the results. Section 4 compares and discusses the results with regards to previous studies. Section 5 concludes the results.

2. Data and Analysis Method

2.1. Rayleigh Lidar and Data

The 532 nm Rayleigh lidar used in this study was developed by the Institute of Atmospheric Physics, Chinese Academy of Sciences, with an Nd:YAG laser as the main transmitting unit. The receiving unit is a main focus telescope with a diameter of 1 m, and a field of view of 1.3 mrad. The data of the lidar system have been verified with high reliability [40,41]. The raw data have a spatial resolution of 30 m and a temporal resolution of 1 min. In order to obtain a sufficient signal-to-noise ratio to detect atmospheric temperature perturbation, the original lidar data are integrated and retrieved to obtain the atmospheric temperature profiles with the spatial resolution of 0.5 km and the temporal resolution of 1 h. The observation data less than 5 h and the uncertainty higher than 5 K are removed. A total of 135 nights and 1174 h of temperature profiles are used, and the monthly distribution of data is shown in Table 1. The mean observation duration time of the daily nocturnal data is 8.7 h. It forms the most extensive high-resolution mesosphere lidar dataset in Golmud and covers seasonal variation. Therefore, this dataset is very suitable to study the characteristics of atmospheric density, temperature and AGWs' activity.

Table 1. The monthly distribution of the lidar data.

2013	January	February	March	April	May	June	July	August	September	October	November	December	Total
Observations hours/h												6 61	6 61
2014	January	February	March	April	May	June	July	August	September	October	November	December	Total
Observations hours/h	5 45					2 14	11 83	9 71	10 82	17 156	14 134	18 180	86 765
2015	January	February	March	April	May	June	July	August	September	October	November	December	Total
Observations hours/h				5 34	5 39		11 82	8 60	1 8	13 125			43 348

2.2. Analysis Method

Typically, the features of AGWs are obtained by extracting the temperature perturbations $T'(z, t)$; refer to the method of Gardner et al. (2007) [42]

$$T'(z, t) = T(z, t) - T_0(z, t) \quad (1)$$

where $T(z, t)$ is the observed temperature and $T_0(z, t)$ is the background temperature. $T_0(z, t)$ is obtained by fitting a straight line over time to the temperature data at each altitude. This method can obtain the characteristics of fluctuations whose period is less

than the observation time of the day and greater than 2 h, and the fluctuation of this scale is mainly contributed by AGWs. $T_0(z, t)$ contains the variation trend of atmospheric temperature with time, so it can effectively eliminate the influence of long-period waves (such as tidal waves and planetary waves) and AGWs whose period is longer than the observation time of the day.

The detrend method above cannot remove the tides absolutely when applied only in the nocturnal dataset. It will suffer from high estimates of GWPED when applied in nocturnal dataset in the mesosphere and lower thermosphere within 84–100 km [17], where the diurnal and semidiurnal tides are strong. However, below 80 km the tides' amplitudes decrease a lot versus decreasing height, and especially below 70 km, they are too small and should be neglected when compared to AGW' activities. It can be inferred that tides will have very small influences on GWPED estimation below 70/80 km [43,44].

Then, the GWPED is calculated by the temperature perturbation, including the potential energy mass density $E_{pm}(z)$ and the potential energy volume density $E_{pv}(z)$

$$E_{pm}(z) = \frac{1}{2} \frac{g^2}{N^2(z)} \overline{\left(\frac{T'(z, t)}{T_0(z, t)} \right)^2} \tag{2}$$

$$E_{pv}(z) = \rho_0(z) E_{pm}(z) \tag{3}$$

where the gravitational acceleration g is taken as 9.7 m/s^2 , $\rho_0(z)$ is the average density of the background atmosphere and the Brunt–Väisälä frequency N is defined as [45]

$$N^2(z) = \frac{g}{T_0} \left(\frac{dT_0(z)}{dz} + \frac{g}{C_p} \right) \tag{4}$$

where $dT_0(z)/dz$ is the background temperature gradient and $C_p = 1004 \text{ J/K/kg}$ is the constant pressure specific heat of dry air.

The uncertainty associated with E_{pm} , σE_{pm} is calculated as follows

$$\sigma^2 E_{pm} = \left(\frac{\partial E_{pm}}{\partial T'} \right)^2 \sigma^2 T' + \left(\frac{\partial E_{pm}}{\partial N^2} \right)^2 \sigma^2 N^2 + \left(\frac{\partial E_{pm}}{\partial T_0} \right)^2 \sigma^2 T_0 \tag{5}$$

Compared to the magnitude order of E_{pm} , $\sigma^2 E_{pm}$ is not significant. E_{pm} can be precisely estimated when using multiple profiles and sufficient data. Therefore, the uncertainty associated with E_{pm} is ignored. Similarly, the uncertainty of E_{pv} is no longer considered.

Assuming that the monochromatic linear AGWs do not exchange energy with the background atmosphere, the potential energy mass density of the conservative AGWs is

$$E_{cov}(z) = E_{pm}(z_0) \exp\left(\frac{z - z_0}{H}\right) \tag{6}$$

$$H = -\left(\frac{d \ln \rho}{dz}\right)^{-1} \tag{7}$$

where H is the atmospheric density scale height, and the classic value is around 7 km; $\exp\left(\frac{z - z_0}{H}\right)$ is a conservative growth rate. When E_{pm} grows away from (less than) the conservative growth rate, dissipation of the waves is the main reason, which will be discussed in Section 3. The departure from the conservative growth rate is quantified by defining the potential energy mass density scale height H_{pm}

$$E_{pmz} = E_{pmz_0} \exp\left(\frac{z - z_0}{H_{pm}}\right) \tag{8}$$

According to the definition of Equation (8), H_{pm} is an indicator of energy dissipation. When H_{pm} is higher than H , it means that the growth rate of E_{pm} is less than the conserva-

tive growth rate, which means that the dissipation of the AGWs occurs. The higher positive value of H_{pm} means that the AGWs are dissipated more seriously [33,37].

3. Results of the Analysis

3.1. Example of the Gravity Waves

Taking the data of 27 October 2014 as an example, the continuous 11 h mesospheric temperature data are used to display the characteristics of AGWs and the derivation of GWPED. Figure 1a shows the temporally averaged profile at 50–80 km, which decreases with altitude from 251.2 K at 50 km to 196.8 K at 80 km, with a temperature drop of 21.7%, and the temperature gradient decreases significantly between 71–75 km. The temperature uncertainty increases from 0.1 K to 0.7 K with altitude. Figure 1b shows the obvious temperature perturbation characteristics of downward phase progression, which means that energy is transferred upward. The vertical wavelength of the monochromatic gravity wave in the observation range of this day is ~ 16.7 km, and the period is ~ 8 h.

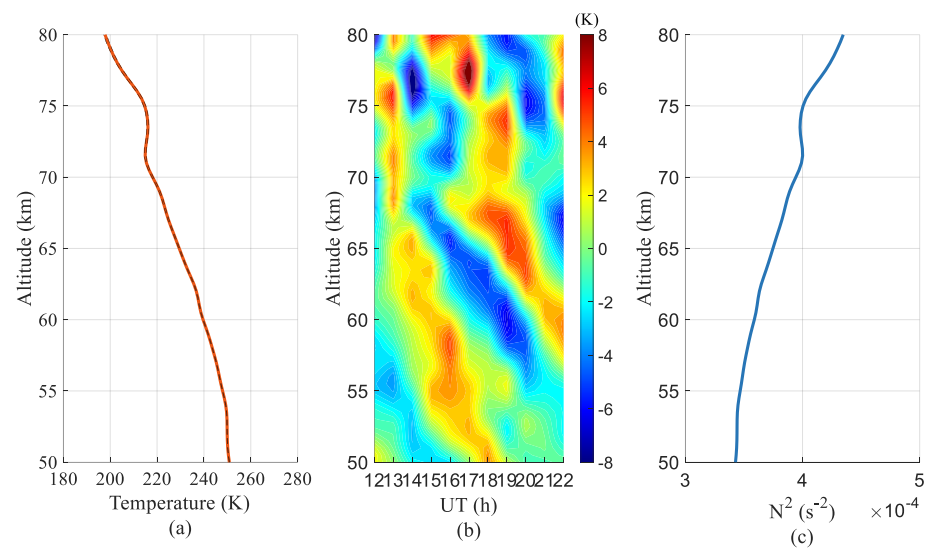


Figure 1. Temperature profile (a), temperature perturbation (b) and N^2 profile (c) on 27 October 2014.

Figure 2 shows the RMS of temperature perturbation and GWPED profiles. The temperature perturbation and the E_{pm} shows an increasing trend with the altitude, and the E_{pv} shows a decreasing trend. In the observation range, the temperature perturbation increases by ~ 2.5 times, and E_{pm} increases by ~ 7.8 times. This difference is caused by the square term of the temperature perturbation in Equation (2) for calculating E_{pm} , and E_{pm} can show the fluctuation more obviously. The AGWs shown in Figure 2b near conservative propagation between around 50–60 km. The energy of the AGWs is weakened compared to the conservative AGWs (dotted line) between 60–69 km. This phenomenon suggests that the energy of the AGWs is dissipated as in the literature [25,37]. The E_{pm} is reduced by ~ 94.7 J/kg compared to the conservative AGWs at 69 km, and it then approaches conservative propagation above 69 km. In Figure 2c, E_{pv} remains stable with altitudes below 60 km and above 69 km, which proves that the AGWs in this altitude range are close to conservative propagation, while the AGWs between 60–69 km are dissipated.

3.2. Characteristics of the GWPED

In order to study the distribution characteristics of GWPED at different altitudes above Golmud, histogram statistics were carried out on E_{pm} results at 50 km, 60 km, 70 km and 80 km as shown in Figure 3, respectively. Figure 3 shows the distribution histograms of the E_{pm} logarithms at several altitudes. The E_{pm} follows a log-normal distribution at all altitudes with standard deviations between 0.42 and 0.47. This is similar to the findings

of N. Mz e’s research [25]. It can be clearly observed that the mean value of $\log_{10}(E_{pm})$ increases from 0.42 at 50 km to 1.71 at 80 km with altitude.

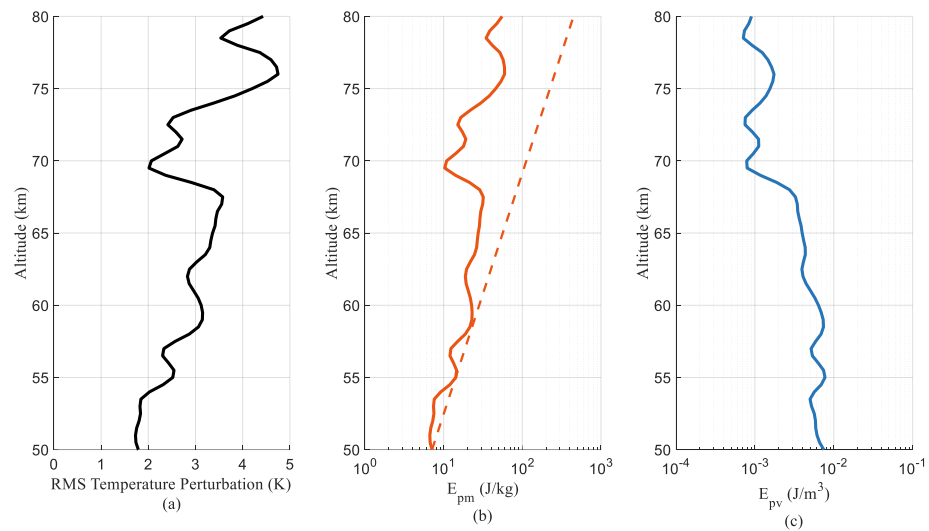


Figure 2. Temperature perturbation RMS profile (a), potential energy mass density E_{pm} profile and the red dotted line is the E_{pm} profile of the conservative AGWs (b), and potential energy volume density E_{pv} profile (c) on 27 October 2014.

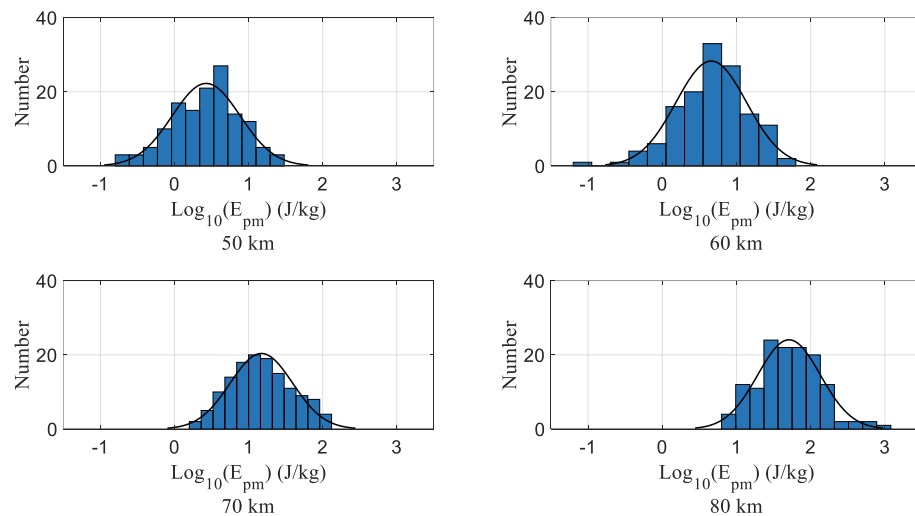


Figure 3. Histograms of the logarithmic distribution of E_{pm} at 50 km, 60 km, 70 km and 80 km in the mesosphere; the black line is the Gaussian distribution fitting of the data.

The averaged GWPED profiles of 1174 h from 2013 to 2015 are shown in Figure 4, in order to study the vertical distribution characteristics of GWPED between 50–80 km above Golmud. E_{pm} increased by an order of magnitude from 4.3 J/kg at 50 km to 86.0 J/kg at 80 km with the altitude, and E_{pv} remained between 10^{-3} – 10^{-2} J/m³. Notice that the E_{pm} profile in Figure 4a shows a significant weakening between 50–61 km. By fitting the E_{pm} of this altitude range, the potential energy mass density scale height H_{pm} is 23.6 km, which is higher than the atmospheric density scale height of 7.3 km. It suggests that the AGWs dissipate and transfer energy into the background atmosphere. At 61 km, E_{pm} is 12.5 J/kg lower than the conservative AGWs. The E_{pv} profile in Figure 4b decreases with altitude below 61 km, and is near constant above 61 km, which also confirms that the dissipation of AGWs above Golmud mainly occurs below 61 km and between 50–80 km.

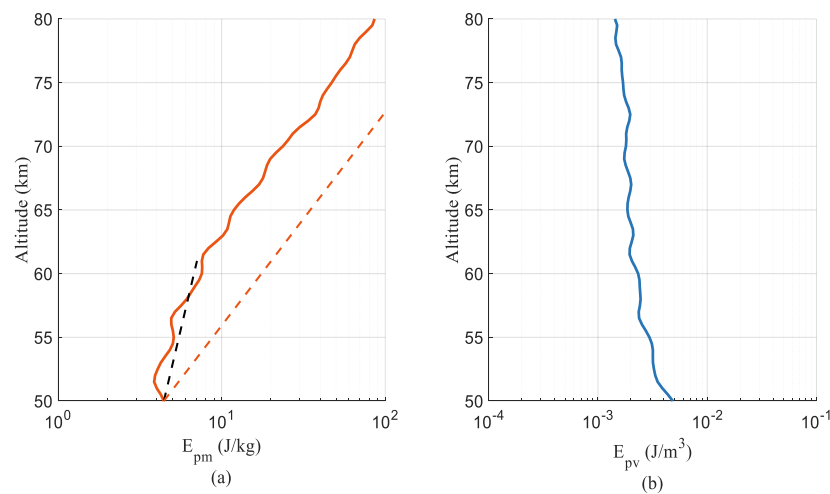


Figure 4. Average profiles of GWPED in 2013–2015. (a) The red solid line is the E_{pm} profile, the red dotted line is the E_{pm} profile of the conservative AGWs, and the black dotted line is the E_{pm} fitting between 50–61 km. (b) The E_{pv} profile.

In order to explore the seasonal variation characteristics of GWPED, this study divided the dataset into spring (March, April, May), summer (June, July, August), autumn (September, October, November) and winter (January, February, December). It should be mentioned that there are no data in February for winter and March for spring as shown in Table 1, which will have some (but not significant) influence on the seasonal statistical results for winter and spring. Since there are two other months data both for the winter and spring statistics, one can take the statistical results below as references to the seasonal variations of GWPED to a large extent. The vertical GWPED profiles for each season are the mean profiles of the GWPED in the observation, and the profiles are smoothed using the Savitzky–Golay filter. The results are shown in Figure 5, and the E_{pm} increased by 17.2, 27.3, 18.6 and 17.0 times with altitude from 3–6 J/kg in each season, respectively. Among these results, the E_{pm} increased faster in summer than other seasons. The GWPED profiles of the four seasons also show severe losses below the turning point and close to conservative growth above it. To analyze the dissipation degree of AGWs in each season, H_{pm} are obtained by fitting the E_{pm} profiles between 50 and 61 km. The results are shown in Table 2. The H_{pm} in summer is the minimum, which means that the dissipation of AGWs in summer is lower than that in other seasons. The H_{pm} results in spring and winter show that the degree of AGWs’ dissipation is more serious between 50–61 km.

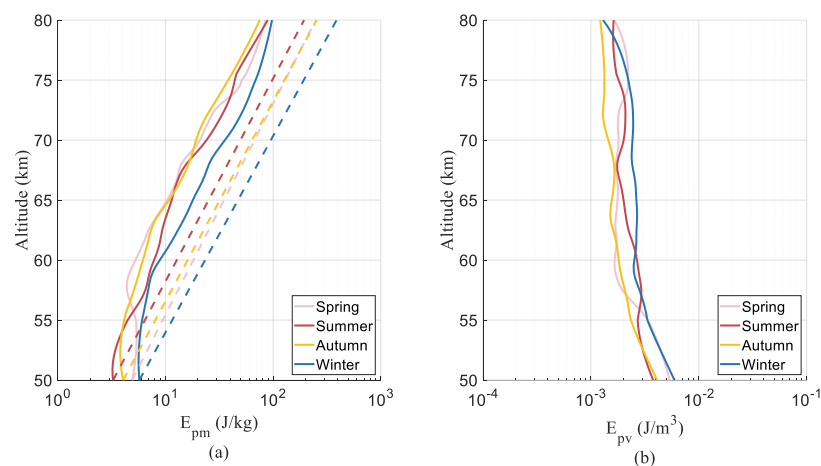


Figure 5. Seasonal average profiles of GWPED. (a) The solid lines are the E_{pm} profiles, and the dotted lines are the E_{pm} profiles of the conservative AGWs. (b) The E_{pv} profiles.

Table 2. Scale Heights (H_{pm} and H).

Scale Heights	Spring	Summer	Autumn	Winter	Total
H_{pm} (km)	58.1	12.6	30.9	47.4	23.6
H (km)	7.6	7.3	7.3	7.1	7.3

4. Discussion

In view of the seasonal characteristics of the GWPED in the mesosphere, most existing studies point out that the peaks appear in winter, but other seasons show different situations. There are many studies that point out that the E_{pm} in the mesosphere is maximum in winter and minimum in summer, including in the mid-latitude regions of the northern hemisphere and the Antarctic region [24,26,28,29,31,33,39]. As shown in Figure 5a, the E_{pm} above Golmud is maximum in winter.

In order to confirm the E_{pm} seasonal characteristics above Golmud, the seasonal average value comparison at different altitude points and monthly contour plot are shown in Figure 6. The study found that in the observation range, the E_{pm} is higher in spring and winter below 55 km, and it is at maximum in winter above 55 km, followed by summer. This feature is similar to the findings of previous studies from locations with similar latitudes. Based on Rayleigh lidar data, the seasonal variation in GWPED between 45–90 km above Logan, Utah (41.74° N, 111.81° W) showed that the E_{pm} is at its maximum in winter below 70 km, followed by summer. [21]. The study of the GWPED vertical distribution above the Haute-Provence Observatory (43.93° N, 5.71° E) between 30–85 km showed that the E_{pm} is at its maximum in winter and summer in the upper mesosphere [25].

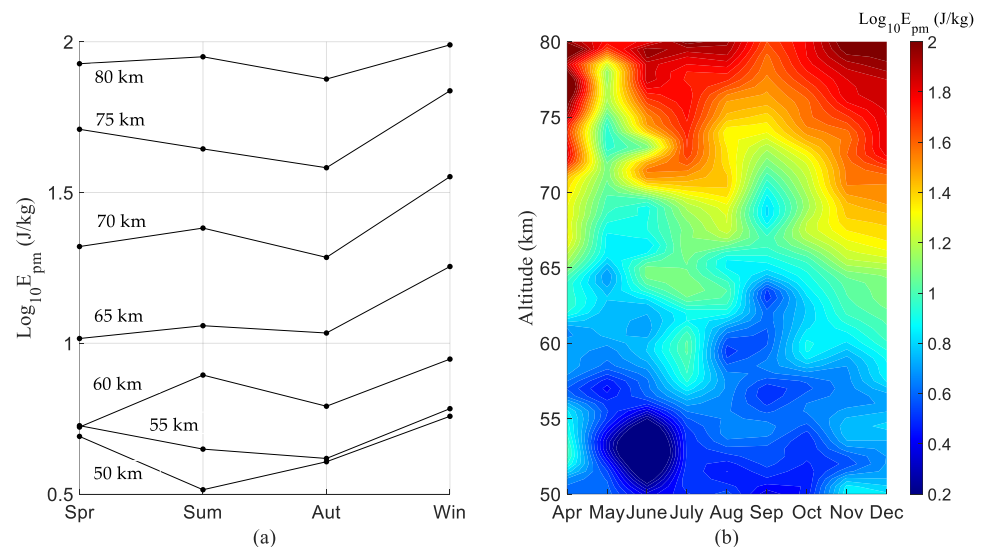


Figure 6. (a) Seasonal averaged E_{pm} at several altitude points. (b) Contour plot of monthly averaged E_{pm} (April to December).

Many studies have shown that the critical level filtering of AGWs by the background wind plays a major role in the seasonal dependence of E_{pm} [25,29]. AGWs encounter a critical level when the phase speed of the wave equals to the mean wind speed [2]. The AGWs observed in the mesosphere are mostly generated in the lower atmosphere. In summer, above mid-latitudes, there is a zero-wind layer of ~20 km between the westerly jet in the lower atmosphere and the easterly jet in the mesosphere, which can filter out the upward propagating mountain waves. In winter, there is no zero-wind layer of ~20 km, and all AGWs can propagate upward into the mesosphere. That may be the main reason why the AGWs' activities are at maximum in winter as observed above. The AGWs' activities show features that are at maximum in winter followed by summer above Golmud, Logan, Utah and the Haute-Provence Observatory in some altitude ranges. The three locations

have similar latitudes but different longitudes. They have different local weather systems (different convective processes, shears, fronts, etc.), which generate different AGWs in the lower atmosphere. Different AGW sources in the lower atmosphere may account for different AGW activities in the mesosphere in summer.

The averaged GWPED profiles in 2013–2015 above Golmud show that AGWs dissipated between 50–61 km and are close to conservative propagation between 61–80 km, as shown in Figure 4. Generally, AGWs are generated in the troposphere and lower stratosphere, which propagate upward [29]. Assuming that the simple linear AGWs propagate upward, the parts of the phase velocity equal to the background wind are filtered and the energy of the AGWs is weakened below 61 km. When AGWs propagate to above 61 km, they are not affected by the critical level and begin to approach conservative propagation. With regard to the study of the dissipation altitude range of AGWs, the study of the Delaware Observatory (42.9° N, 81.4° W) in Canada pointed out that the energy of AGWs is obviously lost in the upper stratosphere [27]. The study between 30–85 km above the Haute-Provence Observatory (43.93° N, 5.71° E) showed that AGWs are significantly dissipated above 70 km [25]. The study of the atmosphere between 45 and 90 km above Logan, Utah (41.74° N, 111.81° W) showed that AGWs approach adiabatic growth rates below 60–65 km and above 75–80 km [21]. Their differences may be due to the different AGW sources and local background winds that influence the AGWs' propagations. The longitudinal dependencies of the AGWs' activities should be significant.

5. Conclusions

In this study, based on the 532 nm Rayleigh lidar of the MARMOT system, a total of 1174 h of temperature profiles in 2013–2015 are used to investigate the GWPED characteristics above Golmud, which is the first Rayleigh lidar observation to research the annual and seasonal variation on GWPED in the mesosphere (50–80 km) of the Tibetan Plateau.

The characteristics of AGWs are obtained by temperature perturbation, and the vertical distribution profiles of potential energy mass density E_{pm} and potential energy volume density E_{pv} are displayed with 0.5 km spatial resolution and 1 h temporal resolution. The distributions of the logarithms of E_{pm} at each altitude points obey the Gaussian distribution. E_{pm} rises by an order of magnitude from 4.4 J/kg at 50 km to 86.0 J/kg at 80 km with altitude. E_{pv} remains in the range of 10^{-3} – 10^{-2} J/m³ and decreases with increasing altitude. The GWPED vertical profiles suggest that the AGWs above Golmud have obvious dissipation in the lower mesosphere and close to conservative propagation in the upper mesosphere, with a turning altitude point at ~61 km. The GWPED presents significant seasonal differences. The E_{pm} increases faster with altitude in summer than others. By calculating H_{pm} , it is shown that the dissipation of AGWs is minimum in summer and more serious in spring and winter. Below 55 km, the E_{pm} is higher in spring and winter, while above 55 km it is maximum in winter, followed by summer. Finally, the AGWs' activities between locations with mid-latitudes and different longitudes are compared and discussed. Comparisons show significant longitudinal dependence.

Author Contributions: Conceptualization, X.H.; methodology, X.H., W.Z. and W.G.; software, W.Z.; validation, X.H., W.P. and Z.Y.; formal analysis, X.H. and W.Z.; investigation, W.Z.; data curation, W.P. and W.Z.; writing—original draft preparation, W.Z.; writing—review and editing, X.H. and W.P.; project administration, W.P.; funding acquisition, W.G. All authors have read and agreed to the published version of the manuscript.

Funding: This work was supported by the Strategic Priority Research Program of the Chinese Academy of Science (Grant XDA17010303 and 17010301) and the National Natural Science Foundation of China (Grants No.41905038, 91952111, 42174192 and 11872128).

Institutional Review Board Statement: Not applicable.

Informed Consent Statement: Not applicable.

Data Availability Statement: Not applicable.

Conflicts of Interest: The authors declare no conflict of interest.

References

1. Fritts, D.C.; Alexander, M.J. Gravity wave dynamics and effects in the middle atmosphere. *Rev. Geophys.* **2003**, *41*, 1003. [[CrossRef](#)]
2. Lindzen, R.S. Turbulence and stress owing to gravity wave and tidal breakdown. *J. Geophys. Res.* **1981**, *86*, 9707–9714. [[CrossRef](#)]
3. Cai, X.; Yuan, T.; Eccles, J.V. A numerical investigation on tidal and gravity wave contributions to the summer time Na variations in the midlatitude E region. *J. Geophys. Res. Space Phys.* **2017**, *122*, 10577–10595. [[CrossRef](#)]
4. Gardner, C.S. Role of wave-induced diffusion and energy flux in the vertical transport of atmospheric constituents in the mesopause region. *J. Geophys. Res. Atmos.* **2018**, *123*, 6581–6604. [[CrossRef](#)]
5. Ba, J.; Hu, X.; Yan, Z.; Guo, S.; Cheng, Y.; Yang, J. Observation analysis on the characteristics of vertical dynamical transport of sodium atoms in the mesopause region over the Langfang area. *Chin. J. Geophys.* **2018**, *61*, 449–457.
6. Alexander, M.J.; Geller, M.; McLandress, C.; Polavarapu, S.; Preusse, P.; Sassi, F.; Sato, K.; Eckermann, S.; Ern, M.; Hertzog, A.; et al. Recent developments in gravity-wave effects in climate models and the global distribution of gravity-wave momentum flux from observations and models. *Q. J. R. Meteorol. Soc.* **2010**, *136*, 1103–1124. [[CrossRef](#)]
7. Geller, M.A.; Alexander, M.J.; Love, P.T.; Bacmeister, J.; Ern, M.; Hertzog, A.; Manzini, E.; Preusse, P.; Sato, K.; Scaife, A.A.; et al. A comparison between gravity wave momentum fluxes in observations and climate models. *J. Clim.* **2013**, *26*, 6383–6405. [[CrossRef](#)]
8. Strelnikova, I.; Almowafy, M.; Baumgarten, G.; Baumgarten, K.; Ern, M.; Gerding, M.; Lübken, F. Seasonal Cycle of Gravity Wave Potential Energy Densities from Lidar and Satellite Observations at 54° and 69° N. *J. Atmos. Sci.* **2021**, *78*, 1359–1386. [[CrossRef](#)]
9. Ern, M.; Trinh, Q.T.; Preusse, P.; Gille, J.C.; Mlynczak, M.G.; Russell, J.M., III; Riese, M. GRACILE. A comprehensive climatology of atmospheric gravity wave parameters based on satellite limb soundings. *Earth Syst. Sci. Data* **2018**, *10*, 857–892. [[CrossRef](#)]
10. Alexander, M.J.; Gille, J.; Cavanaugh, C.; Coffey, M.; Craig, C.; Eden, T.; Francis, G.; Halvorson, C.; Hannigan, J.; Khosravi, R.; et al. Global estimates of gravity wave momentum flux from High Resolution Dynamics Limb Sounder observations. *J. Geophys. Res.* **2008**, *113*, D15S18. [[CrossRef](#)]
11. Ern, M.; Preusse, P.; Alexander, M.J.; Warner, C.D. Absolute values of gravity wave momentum flux derived from satellite data. *J. Geophys. Res.* **2004**, *109*, D20103. [[CrossRef](#)]
12. Bossert, K.; Fritts, D.C.; Heale, C.J.; Eckermann, S.D.; Plane, J.M.C.; Snively, J.B.; Williams, B.P.; Reid, I.M.; Murphy, D.J.; Spargo, A.J.; et al. Momentum flux spectra of a mountain wave event over New Zealand. *J. Geophys. Res. Atmos.* **2018**, *123*, 9980–9991. [[CrossRef](#)]
13. Rauthe, M.; Gerding, M.; Höffner, J.; Lübken, F.J. Lidar temperature measurements of gravity waves over Kuhlungsborn (54° N) from 1 to 105 km: A winter-summer comparison. *J. Geophys. Res.* **2006**, *111*, D24108. [[CrossRef](#)]
14. Alpers, M.; Eixmann, R.; Fricke-Begemann, C.; Gerding, M.; Höffner, J. Temperature lidar measurements from 1 to 105 km altitude using resonance, Rayleigh, and Rotational Raman scattering. *Atmos. Chem. Phys.* **2004**, *4*, 793–800. [[CrossRef](#)]
15. Chanin, M.L.; Hauchecorne, A. Lidar observations of gravity and tidal waves in the stratosphere and mesosphere. *J. Geophys. Res.* **1981**, *86*, 9715–9721. [[CrossRef](#)]
16. Gardner, C.S.; Miller, M.S.; Liu, C.H. Rayleigh lidar observations of gravity wave activity in the upper stratosphere at Urbana, Illinois. *J. Atmos. Sci.* **1989**, *46*, 1838–1854. [[CrossRef](#)]
17. Zhao, J.; Chu, X.; Chen, C.; Lu, X.; Fong, W.; Yu, Z.; Jones, R.M.; Roberts, B.R.; Dörnbrack, A. Lidar observations of stratospheric gravity waves from 2011 to 2015 at McMurdo (77.84° S, 166.69° E), Antarctica: 1. Vertical wavelengths, periods, and frequency and vertical wave number spectra. *J. Geophys. Res. Atmos.* **2017**, *122*, 5041–5062. [[CrossRef](#)]
18. Cai, X.; Yuan, T.; Liu, H.L. Large Scale Gravity Waves perturbations in mesosphere region above northern hemisphere mid-latitude during Autumn-equinox: A joint study by Na Lidar and Whole Atmosphere Community Climate Model. *Ann. Geophys.* **2017**, *35*, 181–188. [[CrossRef](#)]
19. Sivakumar, V.; Rao, P.B.; Bencherif, H. Lidar observations of middle atmospheric gravity wave activity over a low-latitude site (Gadanki, 13.5° N, 79.2° E). *Ann. Geophys.* **2006**, *24*, 823–834. [[CrossRef](#)]
20. Taori, A.; Raizada, S.; Ratnam, M.V.; Tepley, C.A.; Nath, D.; Jayaraman, A. Role of tropical convective cells in the observed middle atmospheric gravity wave properties from two distant low latitude stations. *Earth Sci. Res.* **2012**, *1*, 87–97. [[CrossRef](#)]
21. Kafle, D.N. *Rayleigh-Lidar Observations of Mesospheric Gravity Wave Activity above Logan, Utah*; Utah State University: Logan, UT, USA, 2009.
22. Llamedo, P.; Salvador, J.; Torre, A.; Quiroga, J.; Alexander, P.; Hierro, R.; Schmidt, T.; Pazmiño, A.; Quel, E. 11 years of Rayleigh lidar observations of gravity wave activity above the southern tip of South America. *J. Geophys. Res. Atmos.* **2019**, *124*, 451–467. [[CrossRef](#)]
23. McDonald, A.J.; Thomas, L.; Wareing, D.F. Night-to-night changes in the characteristics of gravity waves at stratospheric and lower-mesospheric heights. *Ann. Geophys.* **1998**, *16*, 229–237. [[CrossRef](#)]
24. Murayama, Y.; Tsuda, T.; Wilson, R.; Nakane, H.; Hayashida, S.A.; Sugimoto, N.; Matsui, I.; Sasano, Y. Gravity wave activity in the upper stratosphere and lower mesosphere observed with the Rayleigh lidar at Tsukuba, Japan. *Geophys. Res. Lett.* **1994**, *21*, 1539–1542. [[CrossRef](#)]
25. Mzé, N.; Hauchecorne, A.; Keckhut, P.; Théti, M. Vertical distribution of gravity wave potential energy from long-term Rayleigh lidar data at a northern middle-latitude site. *J. Geophys. Res. Atmos.* **2014**, *119*, 12069–12083. [[CrossRef](#)]

26. Rauthe, M.; Gerding, M.; Lübken, F.-J. Seasonal changes in gravity wave activity measured by lidars at mid-latitudes. *Atmos. Chem. Phys. Discuss.* **2008**, *8*, 6775–6787. [[CrossRef](#)]
27. Sica, R.J.; Argall, P.S. Seasonal and nightly variations of gravity-wave energy density in the middle atmosphere measured by the Purple Crow Lidar. *Ann. Geophys.* **2007**, *25*, 2139–2145. [[CrossRef](#)]
28. Whiteway, J.A.; Carswell, A.I. Lidar observations of gravity wave activity in the upper stratosphere over Toronto. *J. Geophys. Res.* **1995**, *100*, 14113–14124. [[CrossRef](#)]
29. Wilson, R.; Chanin, M.L.; Hauchecorne, A. Gravity waves in the middle atmosphere observed by Rayleigh lidar: 2. Climatology. *J. Geophys. Res.* **1991**, *96*, 5169–5183. [[CrossRef](#)]
30. Thurairajah, B.; Collins, R.L.; Harvey, V.L.; Lieberman, R.S.; Mizutani, K. Rayleigh lidar observations of reduced gravity wave activity during the formation of an elevated stratopause in 2004 at Chatanika, Alaska (65° N, 147° W). *J. Geophys. Res.* **2010**, *115*, D13109. [[CrossRef](#)]
31. Alexander, S.P.; Klekociuk, A.R.; Murphy, D.J. Rayleigh lidar observations of gravity wave activity in the winter upper stratosphere and lower mesosphere above Davis, Antarctica (69° S, 78° E). *J. Geophys. Res.* **2011**, *116*, D13109. [[CrossRef](#)]
32. Blum, U.; Fricke, K.H.; Baumgarten, G.; Schöch, A. Simultaneous lidar observations of temperatures and waves in the polar middle atmosphere on the east and west side of the Scandinavian mountains: A case study on 19/20 January 2003. *Atmos. Chem. Phys. Discuss.* **2004**, *4*, 809–816. [[CrossRef](#)]
33. Chu, X.; Zhao, J.; Lu, X.; Harvey, V.L.; Jones, R.M.; Becker, E.; Chen, C.; Fong, W.; Yu, Z.; Roberts, B.R.; et al. Lidar observations of stratospheric gravity waves from 2011 to 2015 at McMurdo (77.84° S, 166.69° E), Antarctica: 2. Potential energy densities, lognormal distributions, and seasonal variations. *J. Geophys. Res. Atmos.* **2018**, *123*, 7910–7934. [[CrossRef](#)]
34. Ehard, B.; Achtert, P.; Gumbel, J. Long-term lidar observations of wintertime gravity wave activity over northern Sweden. *Ann. Geophys.* **2014**, *32*, 1395–1405. [[CrossRef](#)]
35. Kaifler, B.; Lübken, F.-J.; Höffner, J.; Morris, R.J.; Viehl, T.P. Lidar observations of gravity wave activity in the middle atmosphere over Davis (69° S, 78° E), Antarctica. *J. Geophys. Res. Atmos.* **2015**, *120*, 4506–4521. [[CrossRef](#)]
36. Li, Z.; Chu, X.; Harvey, V.L.; Jandreau, J.; Lu, X.; Yu, Z.; Zhao, J.; Fong, W. First lidar observations of Quasi-Biennial Oscillation-induced interannual variations of gravity wave potential energy density at McMurdo via a modulation of the Antarctic polar vortex. *J. Geophys. Res. Atmos.* **2020**, *125*, e2020JD032866. [[CrossRef](#)]
37. Lu, X.; Chu, X.; Fong, W.; Chen, C.; Yu, Z.; Roberts, B.R.; McDonald, A.J. Vertical evolution of potential energy density and vertical wave number spectrum of Antarctic gravity waves from 35 to 105 km at McMurdo (77.8° S, 166.7° E). *J. Geophys. Res. Atmos.* **2015**, *120*, 2719–2737. [[CrossRef](#)]
38. Whiteway, J.A.; Duck, T.J.; Donovan, D.P.; Bird, J.C.; Pal, S.R.; Carswell, A.I. Measurements of gravity wave activity within and around the arctic stratospheric vortex. *Geophys. Res. Lett.* **1997**, *24*, 1387–1390. [[CrossRef](#)]
39. Yamashita, C.; Chu, X.; Liu, H.-L.; Espy, P.J.; Nott, G.J.; Huang, W. Stratospheric gravity wave characteristics and seasonal variations observed by lidar at the South Pole and Rothera, Antarctica. *J. Geophys. Res.* **2009**, *114*, D12101. [[CrossRef](#)]
40. Dai, Y.; Pan, W.; Hu, X.; Bai, Z.; Ban, C.; Zhang, H.; Che, Y. An approach for improving the NRLMSISE-00 model using a radiosonde at Golmud of the Tibetan Plateau. *Meteorol. Atmos. Phys.* **2020**, *132*, 451–459. [[CrossRef](#)]
41. Qiao, S.; Pan, W.; Ban, C.; Zhang, H. Mesospheric density measured by Rayleigh lidar over Golmud, Infrared and Laser Engineering. *Infrared Laser Eng.* **2018**, *47*, 23–28.
42. Gardner, C.S.; Liu, A.Z. Seasonal variations of the vertical fluxes of heat and horizontal momentum in the mesopause region at Starfire Optical Range, New Mexico. *J. Geophys. Res. Atmos.* **2007**, *112*, D09113. [[CrossRef](#)]
43. Forbes, J.M. Middle Atmosphere Tides and Coupling between Atmospheric Regions. *J. Geomagn. Geoelectr.* **1991**, *43*, 597–609. [[CrossRef](#)]
44. Zhu, X.; Yee, J.H.; Strobel, D.F.; Wang, X.; Greenwald, R.A. On the numerical modelling of middle atmosphere tides. *Q. J. R. Meteorol. Soc.* **1999**, *125*, 1825–1857. [[CrossRef](#)]
45. Lighthill, J. *Waves in Fluids*; Cambridge University Press: Cambridge, UK, 1978.